Rapid Assessment of Shoreline Changes Induced by Tropical Cyclone Oma Using CubeSat Imagery in Southeast Queensland, Australia

Authors: Kelly, Joshua T., and Gontz, Allen M.

Source: Journal of Coastal Research, 36(1) : 72-87

Published By: Coastal Education and Research Foundation

URL: https://doi.org/10.2112/JCOASTRES-D-19-00055.1

Journal of Coastal Research	36	1	72–87	Coconut Creek, Florida	January 2020

Rapid Assessment of Shoreline Changes Induced by Tropical Cyclone Oma Using CubeSat Imagery in Southeast Queensland, Australia

Joshua T. Kelly[†‡]* and Allen M. Gontz[†]

[†]Department of Geological Sciences
San Diego State University
San Diego, CA 92182, U.S.A.

[‡]Scripps Institution of Oceanography
University of California
San Diego, CA 921093, U.S.A.

www.cerf-jcr.org

www.JCRonline.org

ABSTRACT

Kelly, J.T. and Gontz, A.M., 2020. Rapid assessment of shoreline changes induced by Tropical Cyclone Oma using CubeSat imagery in southeast Queensland, Australia. *Journal of Coastal Research,* 36(1), 72–87. Coconut Creek (Florida), ISSN 0749-0208.

Tropical Cyclone Oma hit the SE Queensland coast of Australia in February 2019. Significant wave heights exceeding 10 m were further amplified by a king tide. Satellite remote sensing of pre- and post-Oma shoreline positions was performed because storms hindered the ability to acquire field-based data. The high spatial and temporal resolution of PlanetScope imagery enabled mapping of the high water line (HWL), which was used as a shoreline indicator across 200 km of shoreline. Given that this is the first use of PlanetScope imagery to map shoreline positions, the positional uncertainty was assessed. Comparison to a temporally coincident, LIDAR-derived mean high water (MHW) shoreline at a distant site showed an average horizontal offset of 9 m with the HWL shoreline. The Oma-affected shoreline uncertainty ranged between ±13.86 and 23.28 m, primarily influenced by the geometric accuracy of the data used, as well as the pixel size of the imagery and the horizontal offset between the HWL and MHW elevations. The net shoreline movement (NSM) was calculated every 200 m along the study area by the Digital Shoreline Analysis System. Only transects with NSM values greater than the uncertainty of their associated shoreline compartment were used to assess change. The spatial distribution of erosion and accretion was similar across the SW–NE-oriented shorelines as the southern ends of Fraser Island and the Cooloola Sand Mass eroded while their northern ends prograded. Wave data shows that the wave direction rapidly shifted 56° in an anticlockwise direction during Oma. Wave propagation came primarily from the SE, and the direction of longshore transport likely turned northward, leading to the shoreline rotation observed in the imagery. This study demonstrates the significant improvement on assessments of regional-scale shoreline changes in the aftermath of an episodic event using new satellite products.

ADDITIONAL INDEX WORDS: *PlanetScope, satellite remote sensing, coastal morphodynamics, Fraser Island, erosion, progradation.*

INTRODUCTION

Coastal systems worldwide are under threat from rising sea level (IPCC, 2014), coastal flooding (Kirshen et *al*., 2008), overdevelopment of the coastal zone (Harvey and Smithers, 2018), and increased storm numbers (Yue *et al*., 2019) and intensity (Putgatch, 2019). As a result, at least 24% of the world's sandy shorelines are eroding at rates surpassing 0.5 m/y (Luijendijk *et al*., 2018), a significant concern for the more than 100 million people living within 1 m of mean sea level (Zhang, Douglas, and Leatherman, 2004). Shoreline erosion affects infrastructure (Laska *et al*., 2005), coastal sites of cultural heritage (Gontz *et al*., 2011; Maio *et al*., 2012) and the recreation carrying capacity of the system (Cisneros *et al*., 2016). Thus, it is critical to understand how coastal systems respond to periods of extreme events.

Advances in satellite technology and geographic information systems provide new mechanisms to examine the effects of episodic events. These techniques couple traditional methods used in aerial photography (Boak and Turner, 2005) and apply new techniques that take advantage of the multispectral capacity of satellite imagery (Kelly and Gontz, 2018; Kelly *et al*., 2019; van der Werff, 2019; Xu, 2018). High-resolution satellite imagery (<5 m/pixel) with high temporal resolution (daily) allows for an unprecedented capacity to track the effect of a single event over large areas without the logistical planning, time, cost, or combination of factors associated with flying low-altitude aerial imagery (Fellman, 2008), beach profiling (Andrade and Ferreira, 2006; Delgado and Lloyd, 2004), or unmanned aerospace systems/unmanned aerial vehicle surveying (Colomina and Molina, 2014; Gonclaves and Henriques, 2015). The assessments can also be achieved from areas remote to the location of the event, increasing the safety of the individuals surveying the area affected. The capacity for rapid assessment of the condition of the coastal system after a major event is critical for management, disaster relief, and safety.

Many early studies that examined the morphological changes to beaches after energetic storms relied on the rudimentary rod and level technique (Fisher and Stauble, 1977; Leatherman, Williams, and Fisher, 1977; Morton, Gibeaut, and Paine, 1995). This labor- and time-intensive survey method typically yielded spatially and temporally deficient datasets that required interpolation of location points between adjacent profiles (Morton, 1991; Overton and Fisher,

DOI: 10.2112/JCOASTRES-D-19-00055.1 received 25 April 2019; accepted in revision 6 August 2019; corrected proofs received 18 September 2019; published pre-print online 9 October 2019.
*Corresponding author: jtkelly@sdsu.edu

1996; Smith and Jackson, 1992). Aerial photography and light detection and ranging (LIDAR) surveys are a significant improvement on manual surveying, because they provide extensive spatial coverage from which quantification of shoreline changes can be assessed, albeit at a much higher acquisition cost that limits temporal resolution (Boak and Turner, 2005; Dolan, Hayden, and May, 1983; Zhang *et al*., 2005). More recently, freely available multispectral satellite imagery has been used to describe shoreline variability over time, although the moderate-resolution of Landsat (30 m) and Sentinel-2 (10 m) imagery limits the accuracy of the interpreted shoreline position and ability to detect smaller scale changes (Hagenaars *et al*., 2018; Pardo-Pascual *et al*., 2014).

These previous shoreline mapping techniques may be found unsuitable for rapid assessments of beach changes induced by high-energy storms because of one or a combination of logistical difficulties, survey costs, and limited spatial resolution. The recent development of small, low-cost satellites known as "CubeSats" potentially represents the next step in assessing the effects of hurricanes and other high-energy storms on global shorelines in near real time (<48 h). The PlanetScope satellite constellation consists of 150 triple CubeSat satellites in a sun-synchronous orbit at an altitude of 475 km. These microsatellites are equipped with a multispectral sensor that acquires imagery in the blue, green, red, and near-infrared wavelength spectrums with a ground sample distance of 3.7 m. Owing to the large number of satellites in orbit, the PlanetScope constellation has been collecting repeat daily coverage of the earth since early 2017. This revelation in satellite technology alleviates the previous tradeoff between high temporal and spatial resolution in a single platform (*i.e*. Landsat). The daily 3.7-m multispectral imagery represents a significant improvement on Landsat's 30-m imagery acquired in 16-day intervals that has been frequently used to assess shoreline changes (Almonacid-Caballer *et al*., 2016; Kelly *et al*., 2019) and could provide much greater insight into storm-induced shoreline changes.

The true definition of a "shoreline" is the physical boundary between land and water (Dolan *et al*., 1980), and a large number of shoreline indicators have been used to delineate its position and to track changes over time (Boak and Turner, 2005). The most commonly used shoreline indicator has been the high water line (HWL), because it is easily identifiable in the field as well as in aerial photography and very high resolution commercial satellite imagery (Anders and Byrnes, 1991; Dolan *et al*., 1980; Moore, 2000; Pajak and Leatherman, 2002); it is identified as the color contrast between the wet intertidal and dry supratidal beach sediment left by the maximum wave runup of the previous high tide (Anders and Byrnes, 1991; Moore, Ruggiero, and List, 2006; Zhang *et al*., 2002). The instantaneous HWL imaged by aerial and spaceborne platforms does not consider the prevailing wind, wave, and tide conditions at the time of capture (Boak and Turner, 2005). Elevated wind speeds and wave heights have been shown to offset the HWL and other shoreline indicators horizontally by tens of meters, particularly on gently sloping beaches (Thieler and Danforth, 1994).

History of Cyclones

Cyclonic storms are a significant threat to coastal environments located within the tropical to subtropical zone. The storms are common in the southwestern North Atlantic and Caribbean oceans, as well as the SE and SW North Pacific Ocean (Bengtsson, Hodges, and Roecker, 2006). In eastern Australia, evidence of large-scale erosion events, like those associated with hurricane or cyclone strikes, was reported from a North Stradbroke Island (Queensland, Australia) ground-penetrating radar survey that showed storm scarps in excess of 2 m occurring on a repetitive basis (Gontz, Moss, and Wagenknecht, 2013). Other studies have shown similar results from beaches throughout Australia (*e.g*., Forsyth, Knott, and Bateman, 2010; Knott *et al*., 2009; May *et al*., 2018). Levin (2011) and Levin, Neil, and Syktus (2014) showed that cyclone activity was responsible for controlling blowout development and renewed activity on the large sand islands. McSweeney and Shulmeister (2018) demonstrated that the shoreline of Rainbow Beach in SE Queensland has experienced large erosive events using repeat aerial photography, and they linked the changes to the El Niño–Southern Oscillation (ENSO). However, their study did not include any pre- and post-storm imagery; thus, erosive episodes could not be linked to specific events. Kelly *et al*. (2019) expanded their work with Landsat imagery over 25 years and showed that long-term shoreline change at the Cooloola Sand Mass is controlled by variability in the Interdecadal Pacific Oscillation (IPO). However, Landsat imagery does not have high spatial resolution; thus, the affects of individual storms also could not be discerned, unless the event resulted in shoreline migration of more than ~15 m. Other documented shoreline changes occurring in response to large-scale storm events not only include erosion and progradation, but washover fan development (May *et al*., 2017; Williams, 2015) and new inlet formation (FitzGerald and Pendleton, 2002; Maio *et al*., 2014).

Tropical Cyclone Oma

Tropical Cyclone Oma (Oma) reached tropical cyclone status on 12 February 2019 at 0000 GMT. The storm was then located at 14° S, 164.5° E, approximately 290 km NW of Vanuatu. Over the next 9 days, the storm slowly moved generally S–SW toward the eastern coast of Australia (Figure 1). During this time, the storm's intensity varied from tropical storm to Category 1 and reached Category 2 on 20 February 2019 at 0400 GMT. On 22 February 2019 at 0000 GMT, the storm intensity had weakened to a Category 1 storm, and the models suggested the storm would stay well offshore of the SE Queensland coast. In response, the tropical cyclone warning for all sections of the SE coast of Queensland and the NW coast of New South Wales (NSW) was canceled. However, as the storm center was approximately 600 km east of the northern section of Fraser Island, hazardous surf and high tide warnings were "still in effect for the next several days" as the storm was expected to intensify to a Category 2, slow, turn north and remain offshore (BOM, 2019). On 22 February 2019, the wave monitoring buoy 50 km east of Point Lookout recorded a 16-m wave and a significant wave height of 10 m. Ultimately, the storm turned east and north in a sharp buttonhook, moving the

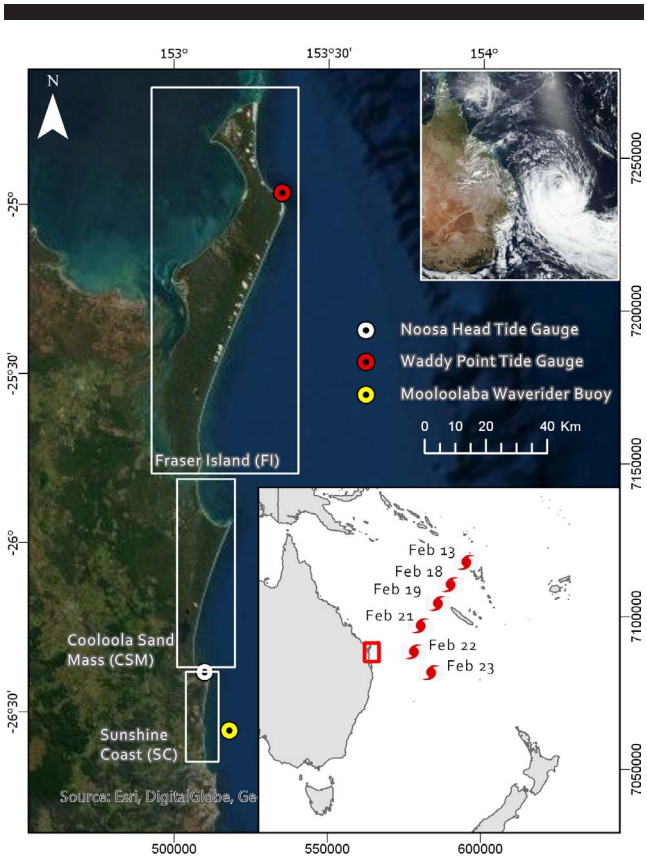

Figure 1. Locations of wave and tide monitoring buoys and the three shoreline study areas: Fraser Island (FI), Cooloola Sand Mass (CSM), and the Sunshine Coast (SC), Queensland, Australia. Inset maps show the geographical context of the study area, the track of Tropical Cyclone Oma, and an image of the storm on 22 February 2019 (courtesy of NASA). DigitalGlobe WorldView imagery was used as the base map. (Color for this figure is available in the online version of this paper.)

storm center farther from the Queensland coast. The storm was off the coast of Queensland for nearly 5 days.

Coupled with Oma, the SE coast of Queensland experienced a king tide on 21 February 2019. Elevated high tide levels resulted in flooding in Brisbane along the Brisbane River (Courier Mail, 2019), beach erosion near Orchid Rock on Fraser Island (J. Shulmeister, *personal communication*, 2019), and a potential for Bribie Island to breach (Redland City Bulletin, 2019). However, the storm did not approach the coast close enough to cause a rainfall event. No precipitation was recorded at the Brisbane Airport (BOM, 2019). Although Oma did not make landfall or approach the coast closer than 450 km, the situation developed conditions that were favorable for large-scale coastal erosion.

Study Site

The coast of SE Queensland is dominated by large sand islands and mainland-attached dune fields (Ellerton *et al*., 2018) that have formed as a result of an extensive longshore transport system that originates in NSW (Boyd *et al*., 2008). Fraser Island (FI), the Cooloola Sand Mass (CSM), and the Sunshine Coast (SC) make up a significant part of this region and represent more than 200 km of predominantly sandy coastline (Figure 1). These sediments are sourced from the Triassic Hawkesbury Sandstone unit located in the Sydney Basin (Wasantha and Ranjith, 2014) and are mostly quartz with <2% heavy minerals and little to no carbonate (Thompson, 1983). The CSM is suggested to be one of the world's oldest continuous coastal dune fields according to thermoluminescence dating of sand grains, revealing an age of 700 ka (Tejan-Kella *et al*., 1990; Walker *et al*., 2018). The mostly open coast shorelines of the study area are wave-dominated and microtidal (Harris *et al*., 2002) and are influenced by a variety of synoptic weather patterns that operate in and around the neighboring Coral Sea (Harley *et al*., 2010). These weather patterns (*i.e*. East Coast Lows, Tropical Cyclones, *etc*.) interact and influence a seasonal wave climate that is highly variable with respect to wave heights and direction (Hemer, McInnes, and Ranasinghe, 2013). Recent work has shown that long-term CSM shoreline dynamics are predominantly controlled by IPO phase variability (Kelly *et al*., 2019).

Purpose

The purpose of this study is twofold: to understand the capabilities and limitations of high spatial and temporal resolution PlanetScope imagery to map shoreline positions and to assess quantitatively shoreline changes induced by Tropical Cyclone Oma in SE Queensland in February 2019.

METHODS

PlanetScope (PS) Analytic Ortho Scene (Level 3B) products were acquired directly from Planet Labs, Inc. These imagery products are orthorectified by ground control points and fine digital elevation models (DEMs) to achieve <10 m root mean square error (RMSE) positional accuracy. Further geometric corrections of the Level 3B imagery are performed by sensor telemetry and attitude telemetry of the spacecraft. The Analytic Ortho Scene products are radiometrically corrected for any sensor artifacts and conversion to absolute radiometric values on the basis of calibration coefficients, which are continuously updated with on-orbit calibration techniques (Planet, 2017). The Level 3B data are provided as both at-sensor radiance and surface reflectance products, of which surface reflectance was used because of the removal of atmospheric artifacts and improved consistency between images acquired at different times. Surface reflectance is calculated with MODIS near–real time aerosol optical depth, ozone, and water vapor parameters sourced from the MOD09-CMA and MOD09CMG datasets. The products are supplied in a WGS84 Universal Transverse Mercator coordinate system (zone 56S for this study area).

Visual inspection of all available PS Analytic scenes in the study area was required to identify scenes with suitable cloud-free coverage along the shoreline area. Data were acquired pre- and post-Oma as close as possible to the storm date, limited primarily by extensive cloud coverage (to be expected during a tropical cyclone). Although no entirely cloud-free days were found, mostly clear days were observed on 15 and 19 February (pre-Oma) and 27 February 2019 (immediately post-Oma). Georectified Level 3B data products were acquired for the study

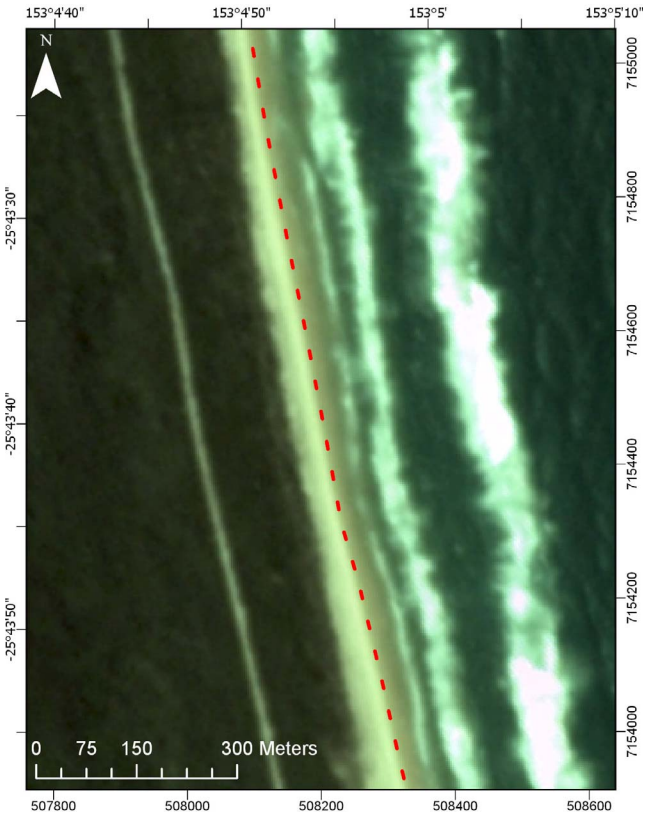

Figure 2. Delineation of the high water line boundary on a PlanetScope RGB composite image. (Color for this figure is available in the online version of this paper.)

area on these dates and used for shoreline delineation. The PS images were imported into ArcGIS Pro and resampled by cubic convolution, which determines each cell value by fitting a smooth curve through the 16 nearest input cell centers. The red (band 3), green (band 2), and blue (band 1) layers contained within each four-band product were composited to create a true color image for visual interpretation. The spatial coverage of the post-Oma imagery is slightly less than the pre-Oma dataset because it does not cover the northernmost 17 km of Fraser Island. Although post-Oma imagery for this region of Fraser Island is available, the data has not been georectified and was opted not to be used in this study. The ~195-km shoreline area analyzed in this study spans 24°51′5″–26°36′41″ S.

The high spatial resolution of the PS imagery enabled the manual digitization of the HWL across the study area for both the pre- and postcyclone image datasets (Figure 2). Interpretation of shoreline areas covered by clouds and shadows was avoided because the contrast difference between the dry supratidal and wet intertidal sand was obscured. Separate shoreline datasets were created for each of the shoreline compartments: FI, CSM, and SC. Multiple shoreline segments mapped within each compartment (separated by uninterpretable areas) were aggregated into a single feature for further analysis.

A LIDAR dataset was acquired from the NSW Government Department of Finance, Services, and Innovation to derive a mean high water (MHW) shoreline position. This datum-based shoreline has become the modern standard for shoreline position estimates (Ruggiero and List, 2009) and is used here to assess the accuracy of the satellite-derived HWL shoreline estimate. The LIDAR dataset covers 12 km of the Gaagal Wanggaan National Park and Carpe Diem Beach coastlines in the Macksville region of NSW. The LIDAR survey occurred between 25 and 28 July 2016, and a cloud-free PS image was acquired only a few days later on 1 August 2016, a short enough time interval to assume no significant geomorphic changes had occurred. An annual average MHW value of 1.421 m was described for the nearby Coffs Harbor recording station (~42 km N of Gaagal Wanggaan) for the period 1990–2010 (MHL, 2012). A MHW shoreline was derived from the LIDAR dataset by extracting elevation values equal to 1.421 ± 0.05 m.

The Digital Shoreline Analysis System (DSAS; Thieler *et al.*, 2017) was used in ArcMap 10.5.1 to quantify the horizontal change in shoreline position pre- and post-Oma, as well as to calculate the average horizontal offset between the HWL and MHW shoreline positions. In preparation for analysis for DSAS, the two shorelines were merged into a single feature class and an attribute table was populated according to Himmelstoss (2009). A baseline used to cast alongshore measurement transects was created by buffering the post-Oma and MHW shorelines 250 m landward. Transects were then cast perpendicular to the shorelines and spaced 200 m apart along the 183-km Oma shoreline (Figure 3; total of 915 measurement transects) and 10 m apart along the 12-km validation shoreline (1228 transects). The migration of the shoreline post-Oma is assessed by calculating the net shoreline movement (NSM) for each of the 915 transects. A total horizontal error for the PS HWL shoreline position is reported as the mean offset from the MHW shoreline.

Although a robust positional error is assessed by comparison with a datum-based MHW position and likely provides a suitable uncertainty benchmark for using PS-derived HWL shorelines, survey data were not available to assess the uncertainty of the Oma shorelines because the most recent LIDAR survey was conducted before the launch of the PS satellites (late 2015). As such, the uncertainty of the pre- and post-Oma shoreline positions are quantitatively assessed following the methods of Hapke *et al.* (2006) and Ruggiero and List (2009). Total shoreline position uncertainty accounts for errors from: (1) georeferencing (source accuracy), (2) source pixel size, and (3) shoreline position uncertainty from water level variations ("proxy-offset bias"; Ruggiero and List, 2009). The proxy-offset bias, or horizontal offset between the HWL and MHW shoreline positions, is estimated by Equation 1:

$$\text{Bias} = (X_{\text{HWL}} - X_{\text{MHW}}) = \frac{\left| Z_{\text{T}} + 1.1 \left\langle 0.35 \tan\beta^2 (H_0 L_0)^{1/2} + \left\{ \left[H_0 L_0 (0.563 \tan\beta^2 + 0.004) \right]^{1/2} \right\} / 2 \right\rangle \right| Z_{\text{MHW}}}{\tan\beta} \quad (1)$$

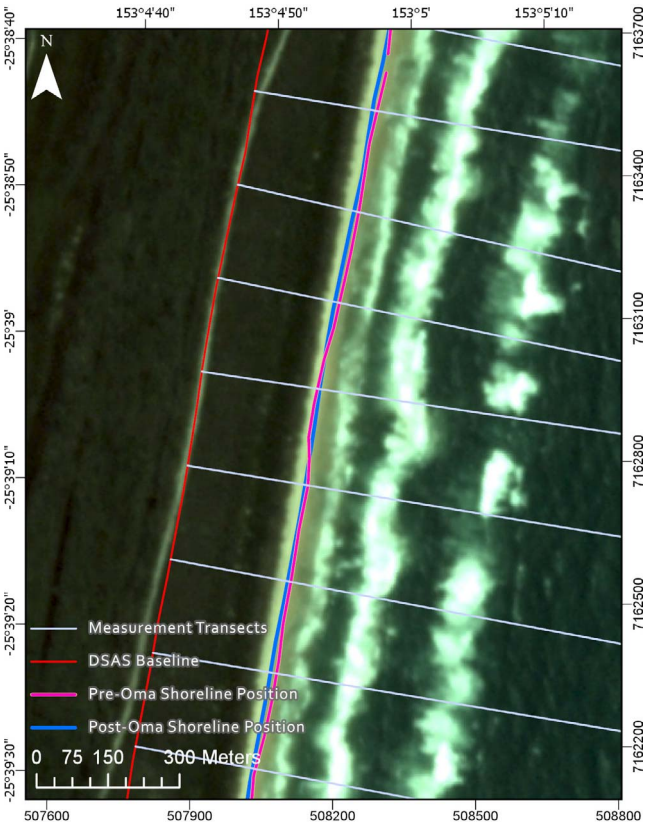

Figure 3. Components of the Digital Shoreline Analysis System: pre- and post-storm shoreline positions, baseline constructed landward of the shoreline dataset, and measurement transects cast every 200 m alongshore from the baseline. (Color for this figure is available in the online version of this paper.)

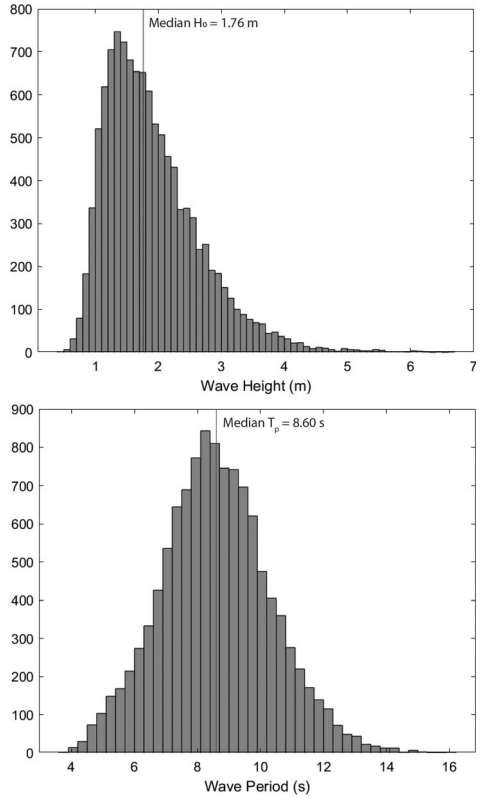

Figure 4. Thirty-one–year (1979–2009) wave height (m) and period (s) record from the NOAA WAVEWATCH III (WWIII) hindcast dataset used to calculate median H_0 (1.76 m) and T_p (8.60 s) values.

where, Z_T is the tide level at the time of survey, tan β is the foreshore beach slope, H_0 is the offshore wave height, L_0 is the deep-water wave length, given by linear theory as $(g/2\pi)/T^2$, where g is the acceleration of gravity and T is the wave period.

Following Ruggiero and List (2009), the long-term median wave height and wavelength were used to calculate the best bias estimate. A 31-year (1979–2009) wave record from the National Oceanic and Atmospheric Administration (NOAA) WAVEWATCH III (WWIII) hindcast dataset was used to calculate median H_0 and T_P values (Figure 4). The WWIII hindcast record has been widely used because of its good agreement with *in situ* wave buoy data (Hemer, Church, and Hunter, 2007; Hughes and Heap, 2010). The 31-year record provided for this study by McSweeney and Shulmeister (2018) was selectively acquired from the 25.90° S, 153.73° E grid point because of its proximity to the coast, yet still uninhibited wave passage. The elevation of mean high water (Z_{MHW}) was estimated to be the average of long-term MHW neap and MHW spring tide elevations provided by the State of Queensland Department of Transport and Main Roads for tidal datum epoch 1992–2011. The tide elevation at the time of image acquisition (Z_T) was interpolated from daily low/high tide records provided by the Commonwealth of Australia Bureau of Meteorology. The closest Queensland Standard Ports to each shoreline compartment were used, which included Waddy Point (24°58′ S, 153°21′ E) for FI and Noosa Head (26°23′ S, 153°06′ E) for CSM and SC.

Because of the unavailability of beach profile data, LIDAR data were used to calculate an average foreshore beach slope (tan β) for each of the three shoreline compartments. A 1-m-resolution LIDAR dataset was acquired from the State of Queensland Department of Natural Resources, Mines, and Energy (survey conducted in 2009). Three polygons defining the spatial extent of the foreshore zone at each compartment were digitized with very high resolution (0.5-m) DigitalGlobe imagery and used to clip the DEM. The slope of each cell located within the foreshore DEM was calculated in ArcGIS Pro, as shown for a stretch of SC in Figure 5. The mean foreshore slope values for FI, CSM, and SC were used to calculate the proxy-offset bias for each shoreline compartment.

The total estimated shoreline position uncertainty (E_{sp}) for the FI, CSM, and SC shoreline compartments was estimated following the method of Hapke *et al*. (2006) and Cenci *et al*. (2013). The total error is estimated by taking the square root of the sum of the squares of georeferencing error (E_g), source pixel

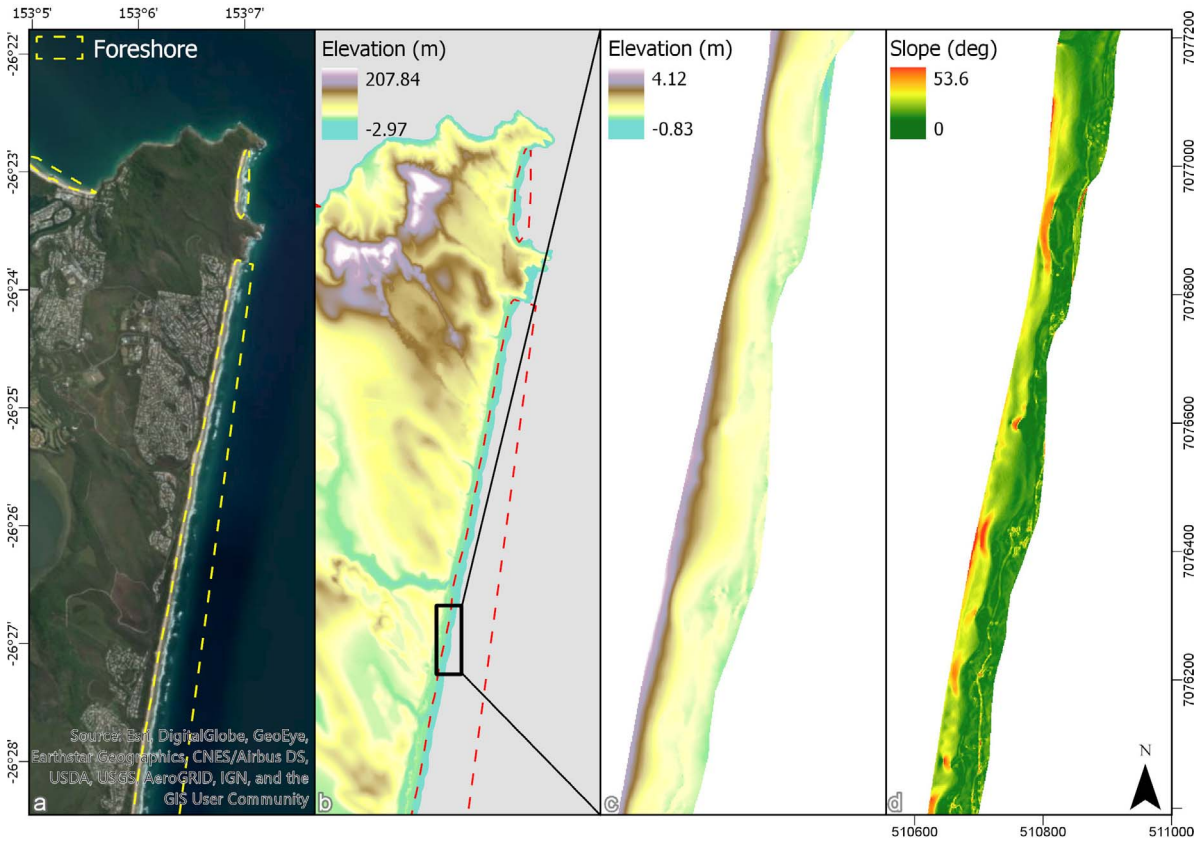

Figure 5. Process of deriving average foreshore slope values from LIDAR data. (a) Manual delineation of the foreshore area in very high resolution WorldView imagery. (b) DEM derived from the LIDAR point cloud data. (c) Extraction of the DEM for the mapped foreshore area. (d) Slope calculation for every cell located in foreshore. (Color for this figure is available in the online version of this paper.)

error (E_{GSD}), and proxy-offset bias (E_p), as shown by Equation 2:

$$E_{sp} = \sqrt{E_g^2 + E_{GSD}^2 + E_p^2} \quad (2)$$

Per Hapke *et al*. (2006), the georeferencing error (E_g) is the maximum RMSE for the data source, which is defined as 10 m for PS imagery (Planet, 2017). The source pixel error is equal to the pixel size of orthorectified PS imagery (3 m) and is included because features smaller than the pixel size cannot be resolved (Cenci *et al*., 2013). Only transects with NSM values greater than the $\pm E_p$ of their associated compartment were considered valid and were used to describe Oma-induced shoreline change. The greater of the two E_p values for the pre- and post-Oma images at each compartment was used as the uncertainty threshold.

Wave monitoring data were acquired to understand the interaction between the Oma-enhanced wave climate and the observed shoreline change. The Mooloolaba Waverider buoy is located offshore of Coolum Beach at the southern extent of the SC (26°33.960′ S, 153°10.870′ E; Figure 1) in 32 m of water depth and is jointly operated by the State of Queensland Department of Environment and the Department of Transport and Main Roads. The buoy acquires a suite of wave climate parameters such as significant wave height, maximum wave height, wave period, wave direction, and sea surface temperature at a 30-minute interval. A record spanning 1 January 2019 through 28 February 2019 was acquired to characterize the Tropical Cyclone Oma wave climate.

RESULTS

The absolute positional uncertainty of a PS-derived shoreline was assessed by comparison with a contemporaneous MHW shoreline derived from a 1-m LIDAR dataset (Figure 6). The horizontal offset between the HWL and MHW shorelines along the 12-km study area ranged from 0.01 to 22.06 m with an average offset of 9.02 m. The MHW shoreline position was almost ubiquitously landward of the HWL shoreline, in that only 36 of the 1227 (3%) measurement transects recorded a negative NSM value.

Storm events in SE Australia are typically defined as waves exceeding 3 m significant wave height (Harley *et al*., 2010). This threshold was only achieved during Tropical Cyclone Oma and, more specifically, from 21 February at 2130 Australian Eastern Standard Time (AEST) to 25 February at 0000 AEST (Figure 7). The mean significant wave height (H_s) during Oma (3.14 m) was more than double the 2-month mean H_s leading up to the storm event (1.54 m) with a maximum H_s of 4.21 m

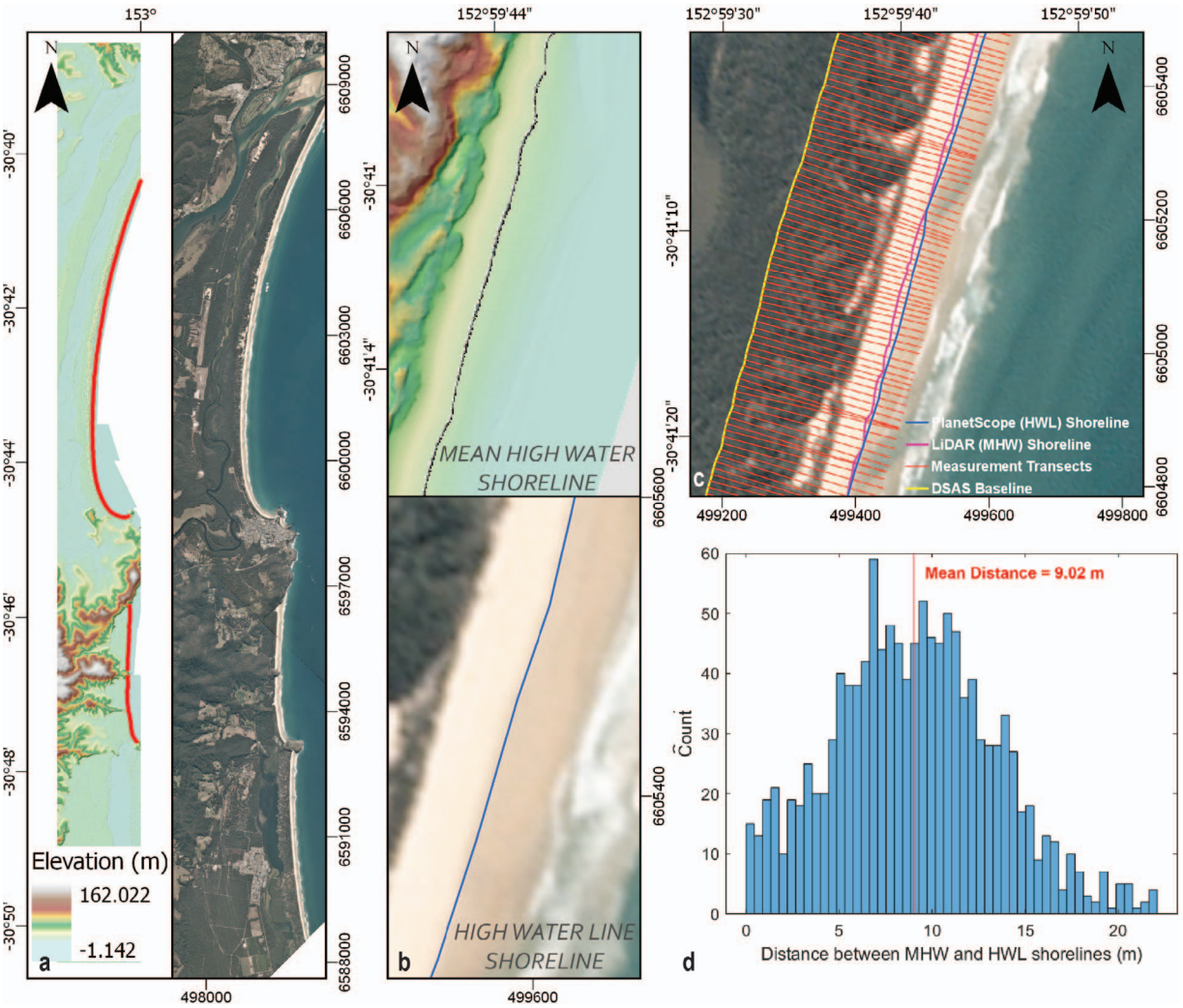

Figure 6. (a) LIDAR and PlanetScope imagery used to extract MHW and HWL shoreline positions at the validation site (indicated by red line). (b) Extraction of MHW and HWL shorelines. (c) DSAS components showing HWL and MHW shorelines with 10-m–spaced measurement transects. (d) Histogram count of 1227 NSM calculations, indicating an average horizontal offset of 9.02 m. (Color for this figure is available in the online version of this paper.)

recorded on 22 February at 1330 AEST. The average peak wave direction (D_p) during the approximately 3-day storm event was 101.1°, a substantial 11.4° increase over the 2-month mean (89.7°). The peak wave direction ranged over 50° as a sharp anticlockwise rotation in wave direction occurred between 63° and 119° (Figure 7).

The SE Queensland coast analyzed in this study was divided into three separate compartments on the basis of political boundaries (*i.e.* Fraser Island) and broad geomorphic characteristics (*i.e.* the high dune bluffs backing the CSM shoreline *vs.* the predominantly built-up area adjacent to the SC shoreline). A description of the total shoreline uncertainty (E_{sp}) and the geomorphic and metocean characteristics used for each of these compartments is provided in Table 1. The total mapped shoreline length for the pre-Oma shoreline across the entire study area was 183.2 km and for the post-Oma shoreline was 181.5 km, with the remaining 12–14 km of the study area being uninterpretable because of the presence of clouds and cloud shadows masking the HWL boundary. Net shoreline movement was calculated every 200 m alongshore, with negative values representing erosion and *vice versa* for accretion in Figures 8 through 10. Any NSM values that are within the ranges of uncertainty (E_{sp}) were omitted from shoreline change analysis.

Net shoreline movement derived from pre- and post-storm PS imagery showed that the FI shoreline both prograded and eroded during Tropical Cyclone Oma (Figure 8). Areas of significant erosion were clustered in the northern and southern extents of FI. Approximately 53% of the SE–NW-trending Orchid Beach shoreline (16.7 km), located at the northernmost extent of the FI study area, eroded with an average landward movement of 17.4 m and NSM values ranging from –11.99 to –33.4 m. A 12-km, SE–NW-trending stretch at the southern end of Seventy-Five Mile Beach showed significant erosion, with an average NSM of –19.8 m, ranging between –14.25 and

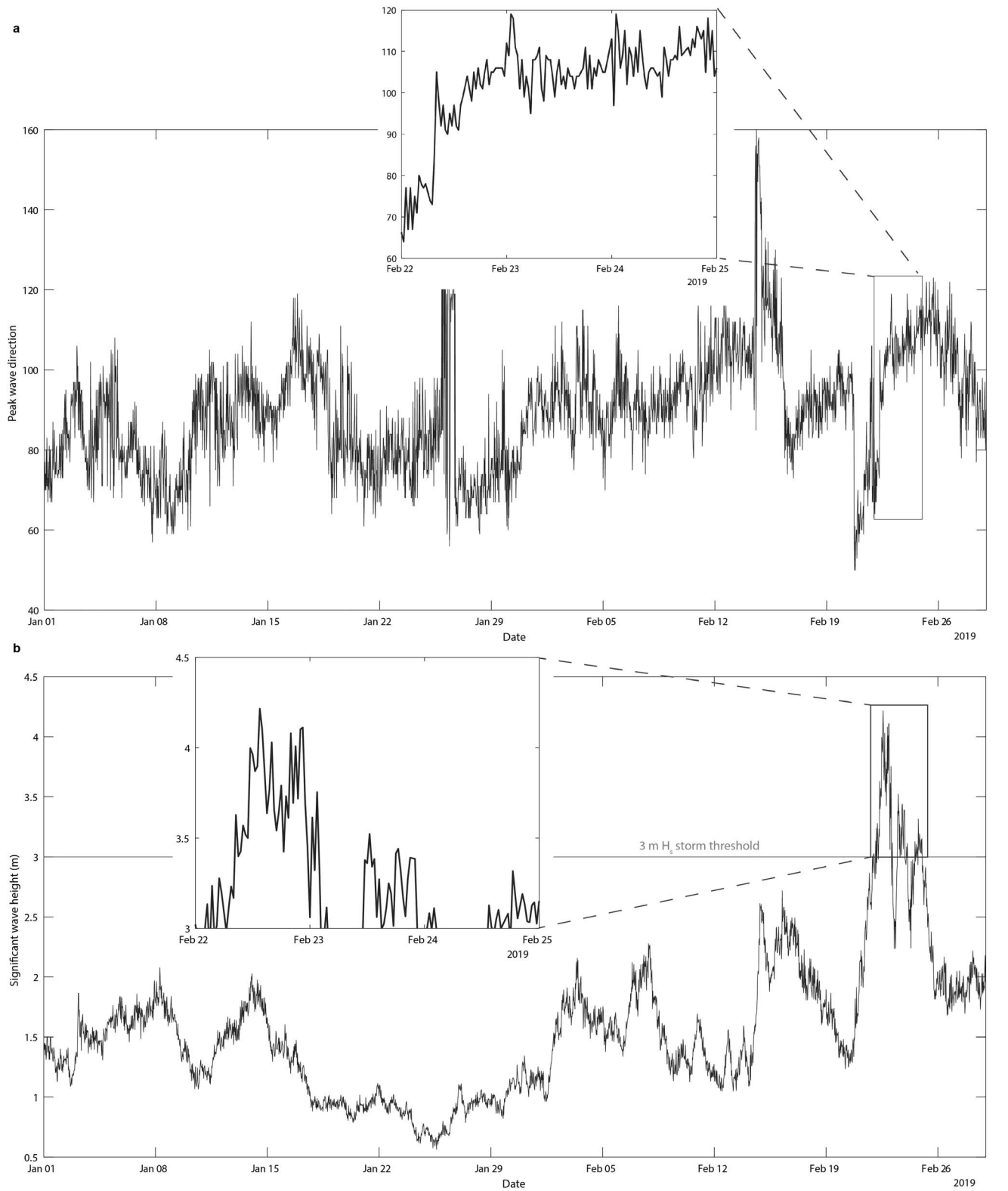

Figure 7. (a) Normal and storm wave directions (degrees from north) measured from the Mooloolaba Waverider buoy from 1 January 2019 to 28 February 2019. Inset plot highlights Oma storm wave directions. (b) Normal and storm significant wave heights (m) as defined by the 3-m H_s threshold.

Table 1. *Geomorphic and metocean characteristics used to calculate the proxy-offset bias (E_p) and total shoreline position uncertainty (E_{sp}) of the three shoreline compartments.*

Shoreline Compartment	Mean tan β	Pre/Post Z_T (m)	Z_{MHW} (m)	Median H_0 (m)	Median T_p (s)	Median L_0 (m)	Pre/Post E_p (m)	E_{sp} (m)
FI	0.029	1.18/0.987	1.62	1.76	8.60	115.35	8.82/3.30	±13.92
CSM	0.035	1.19/1.03	1.62	1.76	8.60	115.35	8.73/3.21	±13.86
SC	0.049	1.79/1.03	1.62	1.76	8.60	115.35	20.65/5.14	±23.28

–31.66 m. Areas of progradation were clustered throughout much of the SW–NE-trending 75 Mile Beach and at the Great Sandy Strait inlet that separates FI from CSM. The northernmost 9 km of 75 Mile Beach prograded an average of 22.1 m within a range of 15.1–34.9 m. A 5-km stretch in the north-central region of 75 Mile Beach prograded an average of 19.6 m within a range of 14.2–29.0 m. A 9-km stretch in the central region of the same beach showed an average progradation of 17.6 m, ranging between 14.4 and 22.9 m. The largest amount of accretion occurred near the Great Sandy Strait inlet, where a

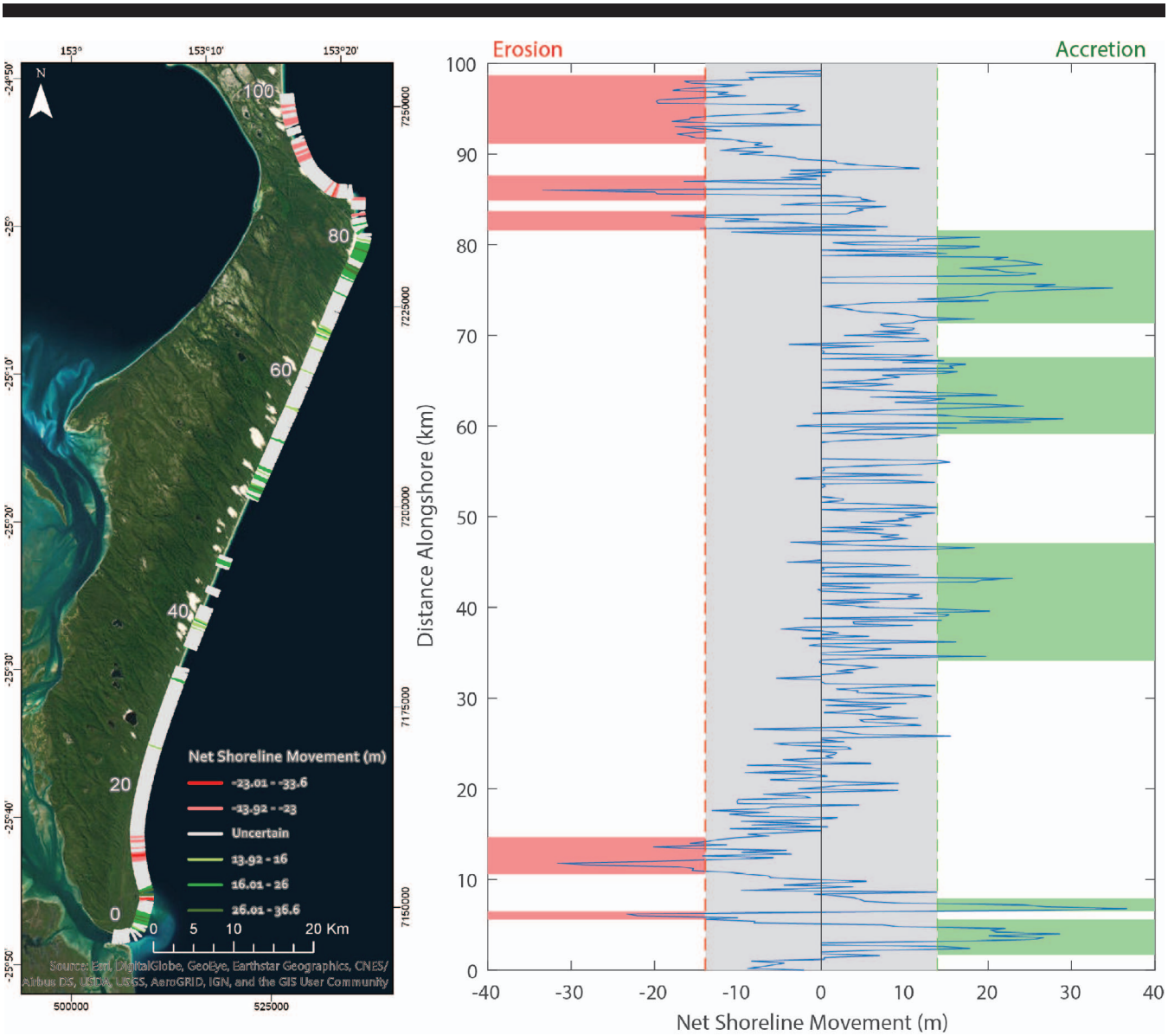

Figure 8. Net shoreline movement across the Fraser Island (FI) study area. Positive NSM values (green) indicate areas of certain progradation, and negative NSM values (red) highlight erosion. The grey region in the plot indicates NSM values within the range of uncertainty (±13.92 m). Numeric values on the map show distance alongshore for correlation to the plot. (Color for this figure is available in the online version of this paper.)

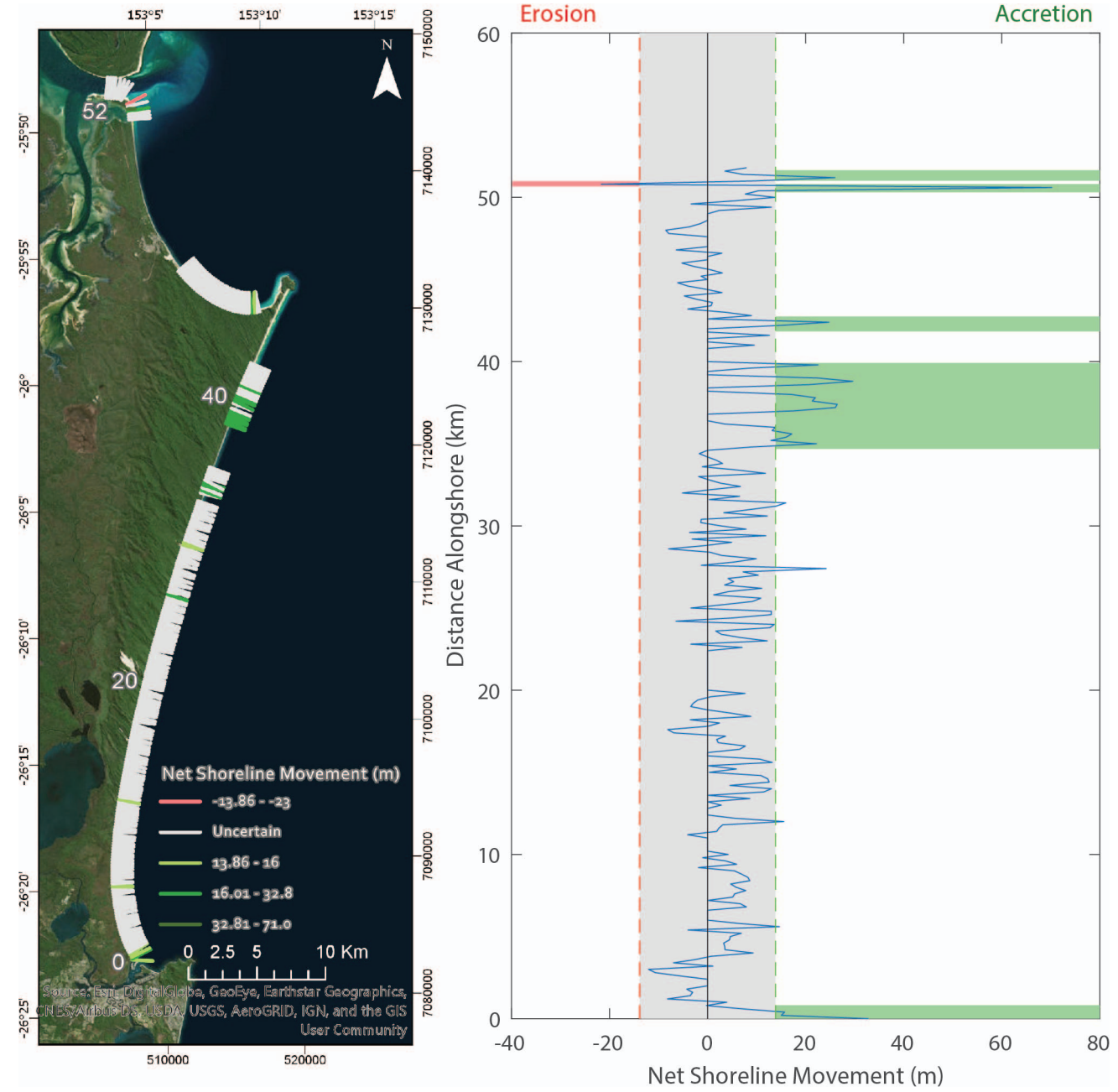

Figure 9. Net shoreline movement across the Cooloola Sand Mass (CSM) study area (uncertainty = ±13.86 m). (Color for this figure is available in the online version of this paper.)

3-km stretch of the shoreline prograded an average of 22.4 m within a range of 14.7–28.6 m. Within this same section, a narrow, 400-m band of erosion amounting to 22.7 m was observed.

Net shoreline movement statistics showed that the CSM mostly prograded in response to Tropical Cyclone Oma (Figure 9). A 1.6-km SE–NW-trending stretch at the northernmost extent of the CSM near the inlet experienced the most extreme shoreline change, predominantly prograding an average of 42.9 m (and a maximum of 70.2 m) with a narrow band of erosion amounting to –21.7 m. Further south, a 500-m stretch located near the Double Island headland shadow zone prograded 19.7 m. The widest area of progradation occurred along the northern end of SW–NE-trending Noosa North Shore, where a 5-km stretch prograded an average of 21.7 m within a range of 16.0–29.7 m. The southernmost 1 km of CSM, bounded by the Noosa River to the south, prograded an average of 19.9 m within a range of 15.0–32.8 m. The significantly higher shoreline

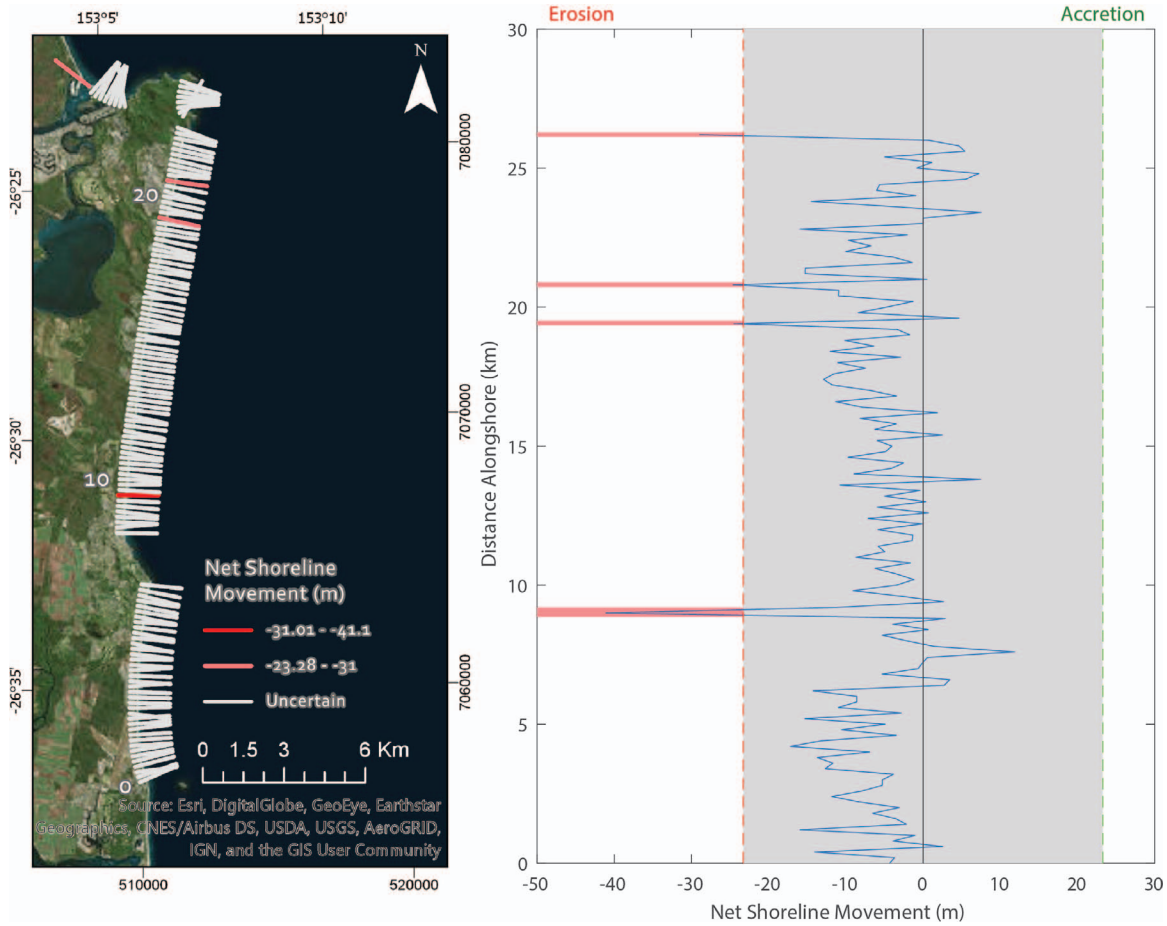

Figure 10. Net shoreline movement across the Sunshine Coast (SC) study area (uncertainty = ±23.28 m). (Color for this figure is available in the online version of this paper.)

position uncertainty for SC (±23.28 m) led to most of the NSM values not being used for shoreline change analysis, although discrete locations of erosion were observed throughout the region and most (>90%) of the uncertain NSM data points indicated erosion (Figure 10). An NSM value of –41.1 m was calculated at the beach fronting the town of Coolum and was aligned with a tidal creek. To the north, two transects with NSM values of –24.6 and –24.5 m indicated significant erosion of the beach bordering the town of Sunshine Beach. Finally, the NW-facing beach at Noosa Spit, which marks the northern terminus of SC, experienced significant erosion with NSM, amounting to –29.0 m.

DISCUSSION

The 3-m imagery provided by the PS constellation proved to be an effective source for mapping the HWL, the most commonly used shoreline indicator in change studies. The color contrast between the dry supratidal and wet intertidal sediment was easily observable in true color composites, which enabled a reliable manual digitization of the shoreline indicator across a large study area for multiple dates. This method represents a significant improvement on previous shoreline change studies that utilized lower spatial resolution satellite imagery, such as Landsat (30 m) and Sentinel-2 (10 m). Where these image products are too coarse to visualize the HWL, spectral water indices such as normalized difference water index (NDWI) and modified NDWI are used to define and track the movement of the shoreline boundary. This mapping technique was found to be significantly influenced by tide height at the time of satellite flyover (Kelly *et al.*, 2019), where interpretation of imagery collected at low tide would show apparent shoreline progradation (and *vice versa* at high tide). The ability to define the HWL in PS imagery removes much of the uncertainty associated with the horizontal movement of the shoreline from tidal variability, which is typically encountered when using water indexing techniques to extract a shoreline boundary.

The response of the three shoreline compartments to the storm wave climate show some similarities, primarily based on the relationship between the orientations of the shorelines and their observed response. The northern ends of the extensive SW–NE-oriented coasts of FI and CSM show significant progradation, where they are both bound by rocky headlands to the north. Concurrently, the southern end of the same coast

on FI that is oriented SE–NW shows similar amplitude erosion. The southern end of CSM also possibly eroded in a similar manner to FI, although the amount of shoreline erosion detected (–12.0 m) is just below the level of local E_{sp} uncertainty (±13.86 m) but beyond the bounds of the MHW offset error (±9 m). Between the southern erosional and northern progradational hot spots, both the FI and CSM shorelines show stable to progradational change in response to Oma. The second, more northern shoreline compartment on FI (Orchid Beach) shows nearly ubiquitous erosion, with the largest retreat amounting to –33.6 m. The orientation of this section is similar to that of the southern erosional area on FI (SE–NW). Although most of the NSM values on SC were omitted because of a much higher uncertainty threshold, areas of significant erosion were detected, and the general trend of the alongshore NSM was erosional. SC does not show the shared southern erosion–northern accretion pattern as FI and CSM, which could be because of its more N–S orientation and exposure to wave incidence.

The rapid and significant anticlockwise rotation in peak wave direction from 63° (incident from the NE) to 119° (incident from the SE) could potentially describe the spatial relationship in erosional and progradational patterns observed in the study area. Previous studies have attempted to describe the geomorphic response of shorelines to changes in ENSO-influenced wave climates (Ranasinghe *et al*., 2004; Short, Trembanis, and Turner, 2000). Ranasinghe *et al*. (2004) show that La Niña phases are associated with a predominantly northeasterly wave direction, which leads to the erosion at the northern end and accretion at the southern end of embayed shorelines in New South Wales (anticlockwise rotation). The opposite is held true during El Niño phases, when a more southeasterly wave climate leads to accretion in the northern end of the same shoreline areas (clockwise rotation).

The same shoreline rotation response likely occurred in the present study area, except at the time scale of days rather than years because of the amplified erosive wave power. As the incident wave direction rotated to the SE, the direction of longshore transport switched from a predominantly southerly direction to the north. The southern ends of FI, and likely CSM, eroded, and the material was transported north along the coast, where it was ultimately deposited from blocking by the Double Island and Waddy Point rocky headlands, leading to significant shoreline progradation. Although spatial coverage of the PS imagery did not allow for analysis of the northern end of Fraser, material eroded from Orchid Beach is likely transported to the northern end of the island and transported over the shelf edge due to uninhibited littoral drift (Boyd *et al*., 2008). The significant progradation observed on the downdrift sides at the inlets of the Great Sandy Strait and Noosa River are likely related to tidal dynamics. This could potentially be due to storm surge–induced ebb channel switching that ultimately released sediment within a few kilometers downdrift of the Great Sandy Strait inlet, as has been observed at other inlets during hurricane conditions (Morton, Gibeaut, and Paine, 1995). Significant erosion of the ebb tidal delta is also likely to occur during storms, mobilizing sediment that is transported and deposited downdrift (Miner *et al*., 2009; Morton, Gibeaut, and Paine, 1995). The inflection point of the shoreline area influenced by tidal dynamics on FI is likely within the 3-km section located 7–10 km alongshore just before the erosive section. The predominantly erosive response of SC could be due to its steeper beach slope that could have reduced wave dissipation in the nearshore zone leading to enhanced wave energy at the shoreline (Vousdoukas *et al*., 2009). Because of this process, offshore transport of beach sediment along SC would cause a reduction in beach slope and significant landward migration of wave runup and the HWL.

In addition to seaward migration of the HWL, geomorphic indicators of shoreline erosion were visually observed in the PS imagery throughout the study area (Figure 11). A 2-km-long sand spit was present along the southern extent of Orchid Beach on the northern half of FI. Much of the pre-Oma sand spit was subaerial on the basis of similar spectral characteristics with the mainland attached beach. A narrow lagoon (50 m at its widest) separated the sand spit from the mainland, and a 15-m-wide inlet breached the spit and connected the lagoon to the Coral Sea. The post-Oma image shows significant infilling of the lagoon, with the remnants taking on the form of "cat's eye" ponds. The once subaerial sand spit appears to have been completely submerged during Oma from the distinctly darker color of the sediment (Figure 11a). Just downdrift from the spit, significant sediment migration over partially vegetated foredune ridges and lagoons is visible in the imagery (Figure 11b). Approximately 2 km of Orchid Beach fronting the identically named seaside resort town experienced significant sand encroachment with an observed maximum migration distance of 61 m. Additionally, significant sediment migration into the Stumers Creek tidal inlet on SC is visible in the post-Oma imagery and is spatially coincident with the southernmost erosive NSM transect (–41.1 m; Figure 11c). In the pre-Oma image, recent channel outflow onto the beach is apparent from the appearance of darker, wet sediment spanning the width of the beach and into the channel. In the post-Oma image, active outflow is no longer evident because the backshore now consists of dry, supratidal sediment that has migrated ~30 m into the Stumers Creek inlet.

The acquisition of global high-resolution imagery at a daily repeat interval has been and will continue to be shown to be paramount in modern and future global change studies. The daily acquisition of PS imagery has already been shown to optimize the timing of harvesting events (Houborg and McCabe, 2018), enhance volcano monitoring (Barnie *et al*., 2018), and aid in global disaster response efforts (Zajic *et al*., 2018). This work shows for the first time that PlanetScope's daily repeat interval allowed for a near-immediate mapping of the shoreline in the aftermath of a significant storm event, enabling a detailed description of storm-induced shoreline change and identification of areas that experienced enhanced erosion or progradation, which is of great interest to local decision makers for shoreline management strategies. The method used here represents a notable improvement in rapidly assessing shoreline changes in the aftermath of a storm event. Previous techniques for describing shoreline change in a rapid response manner are limited by logistical difficulties (expedited mobilization and access to field site) as well as cost (aerial imagery acquisition). The use of satellite imagery for rapid assessment was also previously difficult because of low repeat

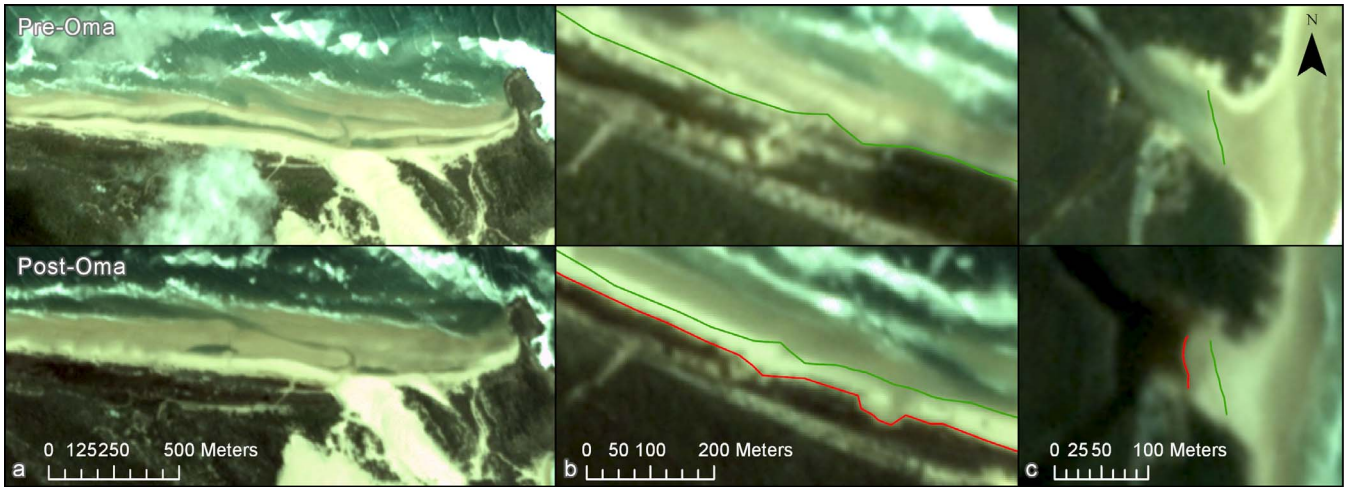

Figure 11. Geomorphic indicators of shoreline erosion. (a) Submergence of a 2-km-long spit and infilling of lagoon at Orchid Beach, FI. (b) Sediment migration over partially vegetated foredune ridges at Orchid Beach, FI. (c) Sediment migration into and blocking of the Stumers Creek tidal inlet at Coolum Beach, SC. (Color for this figure is available in the online version of this paper.)

intervals (5 days for Sentinel-2 and 16 days for Landsat) that would likely be exacerbated if the area of interest was cloud covered during the initial poststorm satellite flyover. Classifying geomorphic changes observed during the subsequent flyover up to 4 weeks after the event ended would likely be imprudent. Although other commercial satellites that acquire near daily very high resolution imagery (*e.g.*, the DigitalGlobe WorldView constellation) have been used to describe shoreline change (Maglione, Parente, and Vallario, 2014; Sekovski *et al.*, 2014), the acquisition cost can be prohibitively expensive.

Although the PS imagery can be used for mapping the HWL on a near daily basis, it is not without its own drawbacks. The PS-derived HWL shoreline shows an average horizontal offset of 9 m from the optimal MHW shoreline position at the validation study site, potentially because of intertidal sediment drying, which would cause an apparent shoreline progradation of the mapped HWL. This situation is likely the cause of the error determined here because 97% of the HWL shoreline was positioned seaward of the MHW shoreline. Regardless, this positional error analysis based on *in situ*, temporally coincident survey data provides a benchmark for future studies that use PS imagery to map and describe shoreline changes over time. This uncertainty value likely will decrease in beach environments with steeper foreshore slopes as the excursion zone is narrowed.

The total shoreline position uncertainty (E_{sp}) of the three Oma study areas omitted 88.3% of the total NSM values because they were within the error of the mapping technique, which ranged between ±13.86 (CSM) and ±23.28 m (SC). This outcome translates to 21.4 km of the 181.5-km-long study area ultimately being retained and used to assess geomorphic changes to the shoreline. A potential source of error in estimating E_{sp} here is the measurements of tan β at each shoreline segment, which was derived from a LIDAR dataset collected in 2009. The E_{sp} of SC was calculated for variable tan β values in an effort to assess its potential variability based on fluctuating foreshore slopes. Stockdon *et al.* (2006) describe oceanographic and geomorphic characteristics of a wide range of natural beaches. They noted that gently sloping (dissipative) beaches with a mean slope of 0.06 can vary by up to ±0.002. Using these upper and lower slope limits, the E_{sp} at SC (20.65 m when tan $\beta = 0.049$) is 0.32 m greater when tan $\beta = 0.047$ (1.3% difference) and 0.57 m less when tan $\beta = 0.051$ (2.4%). As such, variability of tan β should not be considered a significant source of error for calculating E_{sp}, although this may not hold true at steeper, more reflective beaches where significant lowering can occur.

The greatest source of error in the E_{sp} calculations for all but one of the image datasets was the georeferencing error (geometric accuracy) of the PS data product (10 m). Only the pre-Oma dataset for SC had a larger source of error, which was its proxy-offset bias (E_p; 20.65 m). The pre-Oma SC E_p value of 20.65 was the result of an abnormally high tide during the survey on 19 February (Z_T; 1.79 m), which was 0.17 m higher than the Z_{MHW}. Given that the proxy-offset bias is primarily from wave-driven water level variations (setup and swash) driving the horizontal displacement between the HWL and MHW (Ruggiero and List, 2009), E_p is expected to be anomalously large if $Z_T > Z_{MHW}$ and wave runup is amplified. The lowest E_p values were achieved when $Z_T < Z_{MHW}$ (*i.e.* $E_p =$ 3.30 and 3.21 m when $Z_T = 0.99$ and 1.03 m for the post-Oma FI and CSM datasets, respectively) because wave runup during low-to-mid tide positions the HWL close to MHW. Future studies using PS to map shorelines with this technique should consider the tide height during the time of satellite flyover to minimize the position error from the proxy-offset bias. Future improvements on the orthorectification of the PS data products will also significantly improve the shoreline position uncertainty, although its 10-m root mean square geometric accuracy is already an improvement on Landsat 8 (12 m; Roy *et al.*, 2014) and Sentinel-2 (11 m; ESA, 2019).

CONCLUSIONS

Tropical Cyclone Oma was a powerful, Category 2 storm that moved toward the SE Queensland coast over the course of 9 days. Although the storm never made landfall in Australia, it reached within 450 km of Fraser Island, during which time it had weakened to a Category 1 cyclone. The close proximity of the massive storm to the Sand Island coast produced remarkably high surf conditions, as observed by wave monitoring buoys that recorded significant wave heights up to 10 m. These storm surge conditions were amplified by a king tide that resulted in flooding along the Brisbane River. The effects of these extremely energetic oceanographic conditions on the sandy, open-coast shorelines of SE Queensland were assessed with newly available, high temporal and spatial resolution satellite imagery.

The HWL was mapped on the 3-m resolution, multispectral PlanetScope imagery by manually defining the boundary between wet intertidal and dry supratidal sediment. Pre-storm shoreline positions were mapped across the study area from imagery collected 3 and 6 days before the arrival of Oma, and poststorm positions were defined a mere 3 days after the storm wave conditions returned to normal. For the first time, the total shoreline position uncertainty associated with the use of PS imagery to map the HWL was assessed by comparison to a temporally coincident MHW shoreline at a distant validation site and by calculating the proxy-offset bias at the Oma-affected study area. The average horizontal offset between the MHW and HWL shorelines across the 12-km validation site was 9.02 m, with the HWL shoreline nearly entirely seaward of the MHW. The local E_{sp} across the three shoreline compartments ranged from $\pm$13.86 to 23.28 m. Uncertainty of the PS-derived shorelines was primarily due to the geometric accuracy of the Level 3B PS imagery (10 m RMSE), in addition to its pixel size (3 m) and site-specific proxy-offset bias.

Net Shoreline Movement statistics calculated by DSAS show that the FI and CSM both prograded and eroded and SC eroded during Tropical Cyclone Oma. The FI and CSM shorelines display similar spatial patterns in the locations of erosion and accretion. The northern ends of their extensive SW–NE-oriented shorelines experienced significant progradation that was contemporaneous with shoreline erosion at their southern ends with stable to uncertain progradation occurring in between. The wave climate during the three-day storm period (when $H_s > 3$ m) experienced a rapid and significant 56° anticlockwise rotation (from 63° to 119°), likely shifting the mean direction of longshore transport to the north and resulting in clockwise beach rotation, a geomorphic process observed at quasi-biennial time scales because of ENSO phase variability. Although the higher E_{sp} of the SC shoreline omitted most of the NSM values, regions of exceptional shoreline erosion were identified and are theorized to have been due to its steeper beach slopes that lowered because of enhanced wave energy.

This study demonstrates for the first time the capability of using PS imagery to map shoreline positions and detect their horizontal change occurring at a weekly time interval in response to episodic events. The daily repeat interval of the PS satellites allowed for acquisition of mostly cloud-free, georectified imagery 1 week before and after Oma's arrival. This ensured that the significant shoreline changes described by both the migration of the HWL and through direct observation of geomorphic processes were entirely due to Oma. This study also shows that the use of PS imagery significantly improves rapid detection and assessment of shoreline changes in the immediate aftermath of a storm or other powerful event. Previous techniques were limited by prohibitively expensive costs (airborne surveys), logistical difficulties (access to damaged field site), and inadequate temporal coverage (Landsat repeat interval of 16 days). Future improvements in the accuracy of PS-derived shoreline positions can be achieved through enhancement of the geometric accuracy of the PS data products and selective use of images that were acquired at mid to low tide. Automated mapping of the HWL with PS imagery across regional- to continental-scale study areas could be possible with support vector machines and other machine learning classification techniques and is the subject of future work.

ACKNOWLEDGMENTS

We thank Planet Labs, Inc., for providing the PlanetScope imagery through their Education and Research Program, The State of Queensland for supplying tide and wave data, and the NSW Government for providing the LIDAR dataset. This work was carried out within the Joint Doctoral Program in Earthquake Science and Applied Geophysics at the University of California, San Diego, and San Diego State University. The paper was significantly improved by the comments of the two anonymous reviewers.

LITERATURE CITED

Almonacid-Caballer, J.; Sanchez-Garcia, E.; Pardo-Pascual, J.E.; Balaguer-Beser, A.A., and Palomar-Vazquez, J., 2016. Evaluation of annual mean shoreline position deduced from Landsat imagery as a mid-term coastal evolution indicator. *Marine Geology*, 372, 79–88.

Anders, F.J. and Byrnes, M.R., 1991. Accuracy of shoreline change rates as determined from maps and aerial photographs. *Shore and Beach*, 59(1), 17–26.

Andrade, F. and Ferreira, M.A., 2006. A simple method of measuring beach profiles. *Journal of Coastal Research*, 22(4), 995–999.

Barnie, T.; Thrastarson, R.; Jonsdottir, I., and Moussallam, Y., 2018. The Cubesat Revolution in Volcano Monitoring—Examples from PlanetScope. *Proceedings of the 20th EGU General Assembly* (Vienna, Austria), pp. 19580.

Bengtsson, L.; Hodges, K.I., and Roecker, E., 2006. Storm tracks and climate change. *Journal of Climate*, 19(15), 3518–3543.

Boak, E. and Turner, I., 2005. Shoreline definition and detection: A review. *Journal of Coastal Research*, 21(4), 688–703.

Boyd, R.; Ruming, K.; Goodwin, I.; Sandstrom, M., and Schroder-Adams, C., 2008. Highstand transport of coastal sand to the deep ocean: A case study from Fraser Island, southeast Australia. *Geology*, 36(1), 15–18.

BOM (Bureau of Meteorology), 2019. http://www.bom.gov.au/.

Cenci, L.; Disperati, L.; Sousa, L.P.; Phillips, M., and Alve, F.L., 2013. Geomatics for Integrated Coastal Zone Management: Multitemporal shoreline analysis and future regional perspective for the Portuguese Central Region. *In:* Conley, D.C.; Masselink, G.; Russell, P.E., and O'Hare, T.J. (eds.), *Proceedings from the International Coastal Symposium (ICS) 2013*. *Journal of Coastal Research*, Special Issue No. 65, pp. 1349–1354.

Cisneros, M.A.H.; Sarmiento, N.V.R.; Delrieux, C.A.; Piccolo, M.C., and Perillo, G.M.E., 2016. Beach carrying capacity assessment through image processing tools for coastal management. *Ocean & Coastal Management*, 130, 138–147.

Colomina, I. and Molina, P., 2014. Unmanned aerial systems for photogrammetry and remote sensing: A review. *ISPRS Journal of Photogrammetry and Remote Sensing*, 92, 79–97.

Courier Mail, 2019. *Waves surge over seaside path as Cyclone Oma brings high tides to Queensland*, Storyful video, 0:36, 21 February 2019. https://www.couriermail.com.au/news/national/waves-surge-over-seaside-footpath-as-cyclone-oma-brings-high-tides-to-queensland/video/06dfbbf6cc37ee4681d8528d69ab2488

Delgado, I. and Lloyd, G., 2004. A simple low cost method for one person beach profiling. *Journal of Coastal Research*, 20(4), 1246–1252.

Dolan, R.; Hayden, B.P.; May, P., and May, S.K., 1980. The reliability of shoreline change measurements from aerial photographs. *Shore and Beach*, 48(4), 22–29.

Dolan, R.; Hayden, B.P., and May, S., 1983. Erosion of the US shorelines. *In:* Komar, P.D. (ed.), *CRC Handbook of Coastal Processes and Erosion*. Boca Raton, Florida: CRC Press, pp. 285–299.

Ellerton, D.; Rittenhour, T.; Miot da Silva, G.; Gontz, A.; Shulmeister, J.; Hesp, P.; Santini, T., and Welsh, K., 2018. Late Holocene cliff-top blowout activation and evolution in the Cooloola Sand Mass, southeast Queensland, Australia. *The Holocene*, 28(11), 1697–1711.

ESA (European Space Agency), 2019. *S2 MPC L1C Data Quality Report*. Paris, France: ESA *Reference S2-PDGS-MPC-DQR*, issue 36, 3 May 2019, 46p. https://sentinel.esa.int/documents/247904/685211/Sentinel-2_L1C_Data_Quality_Report.

Fellman, J.P., 2008. Visibility mapping in New York's coastal zone: A case study of alternative methods. *Coastal Zone Management Journal*, 9(3–4), 249–270.

Fisher, J.S. and Stauble, D.K., 1977. Impact of Hurricane Belle on Assateague Island washover. *Geology*, 5(12), 765–768.

FitzGerald, D.M. and Pendleton, E.P., 2002. Inlet formation and evolution of the sediment bypassing system: New Inlet, Cape Cod, Massachusetts. *In:* Cooper, J.A.G. and Jackson, D.W.T. (eds.), *Proceedings from the International Coastal Symposium (ICS) 2002*. *Journal of Coastal Research,* Special Issue No. 36, pp. 290–299.

Forsyth, A.J.; Knott, J., and Bateman, M.D., 2010. Beach ridge plain evidence of a variable late-Holocene tropical cyclone climate, North Queensland, Australia. *Palaeogeography, Palaeoclimatology, Palaeoecology*, 297(3–4), 707–716.

Gonclaves, J.A. and Henriques, R., 2015. UAV photogrammetry for topographic monitoring of coastal areas. *ISPRS Journal of Photogrammetry and Remote Sensing*, 104, 101–111.

Gontz, A.M.; Maio, C.V.; Wagenknecht, E.K., and Berkland, E.P., 2011. Assessing threatened coastal sites: Applications of ground penetrating radar and geographic information systems. *Journal of Cultural Heritage*, 12(4), 451–458.

Gontz, A.M.; Moss, P.T., and Wagenknecht, E.K., 2013. Stratigraphic architecture of a regressive strand plain, Flinders Beach, North Stradbroke Island, Queensland, Australia. *Journal of Coastal Research*, 30(3), 575–585.

Hagenaars, G.; de Vries, S.; Luijendijk, A.P.; de Boer, W.P., and Reniers, A.J.H.M., 2018. On the accuracy of automated shoreline detection derived from satellite imagery: A case study of the sand motor mega-scale nourishment. *Coastal Engineering*, 133, 113–125.

Hapke, C.J.; Reid, D.; Richmond, B.M.; Ruggiero, P., and List, J., 2006. *National Assessment of Shoreline Change: Part 3: Historical Shoreline Changes and Associated Coastal Land Loss along the Sandy Shorelines of the California Coast*. Reston, Virginia: U.S. Geological Survey, *Open-file Report 2006-1219*, 72p.

Harley, M.D.; Turner, I.L.; Short, A.D., and Ranasinghe, R., 2010. Interannual variability and controls of the Sydney wave climate. *International Journal of Climatology*, 30(9), 1322–1335.

Harris, P.T.; Heap, A.D.; Bryce, S.M.; Porter-Smith, R.; Ryan, D.A., and Heggie, D.T., 2002. Classification of Australian clastic coastal depositional environments based upon a quantitative analysis of wave, tidal, and river power. *Journal of Sedimentary Research*, 72(6), 858–870.

Harvey, N. and Smithers, S., 2018. How close to the coast? Incorporating coastal expertise into decision-making on residential development in Australia. *Ocean & Coastal Management*, 157, 237–247.

Hemer, M.A.; Church, J.A., and Hunter, J.R., 2007. Waves and climate change on the Australian coast. *In:* Lemckert, C.J. (ed.), *Proceedings from the International Coastal Symposium (ICS) 2007*. *Journal of Coastal Research*, Special Issue No. 50, pp. 432–437.

Hemer, M.A.; McInnes, K.L., and Ranasinghe, R., 2013. Projections of climate change–driven variations in the offshore wave climate off south eastern Australia. *International Journal of Climatology*, 33(7), 1615–1632.

Himmelstoss, E.A., 2009. DSAS 4.0—Installation Instructions and User Guide. *In:* Thieler, E.R.; Himmelstoss, E.A.; Zichichi, J.L., and Ergul, A. (eds.), *The Digital Shoreline Analysis System (DSAS) Version 4.0—An ArcGIS Extension for Calculating Shoreline Change*. Reston, Virginia: U.S. Geological Survey, *Open-File Report 2008-1278*, ver. 4.2. 81, 81p.

Houborg, R. and McCabe, M.F., 2018. Daily retrieval of NDVI and LAI at 3 m resolution via the fusion of CubeSat, Landsat, and MODIS data. *Remote Sensing*, 10(6). doi:0.3390/rs10060890

Hughes, M.G. and Heap, A.D., 2010. National-scale wave energy resource assessment for Australia. *Renewable Energy*, 35(8), 1783–1791.

IPCC (Intergovernmental Panel on Climate Change), 2014. *Climate Change 2014: Synthesis Report. Contribution of Working Groups I, II and III to the Fifth Assessment Report of the Intergovernmental Panel on Climate Change* [Core Writing Team, R.K. Pachauri and L.A. Meyer (eds.)]. Geneva, Switzerland: IPCC, 151p.

Kelly, J.T. and Gontz, A.M., 2018. Using GPS-surveyed intertidal zones to determine the validity of shorelines automatically mapped by Landsat water indices. *International Journal of Applied Earth Observation and Geoinformation*, 65, 92–104.

Kelly, J.T.; McSweeney, S.; Shulmesiter, J., and Gontz, A.M., 2019. Bimodal climate control of shoreline change influenced by Inter-decadal Pacific Oscillation variability along the Cooloola Sand Mass, Queensland, Australia. *Marine Geology*, 415. doi:10.1016/j.margeo.2019.105971

Kirshen, P.; Watson, C.; Douglas, E.; Gontz, A.; Lee, J., and Tian, Y., 2008. Coastal flooding in the northeastern United States due to climate change. *Mitigation and Adaptation for Global Change*, 13(5), 437–451.

Knott, J.; Smithers, S.; Walsh, K., and Rhodes, E., 2009. Sand beach ridges record 6000 year history of extreme cyclone activity in northeastern Australia. *Quaternary Science Reviews*, 28(15–16), 1511–1520.

Laska, S.; Wooddell, G.; Hangleman, R.M.; Grammling, R., and Farris, M.T., 2005. At risk: The human community and infrastructure resources of coastal Louisiana. *In:* Finkl, C.W. and Khalil, S.M. (eds.), *Saving America's Wetland: Strategies for Restoration of Louisiana's Coastal Wetlands and Barrier Islands*. *Journal of Coastal Research*, Special Issue No. 44, pp. 90–111.

Leatherman, S.P.; Williams, A.T., and Fisher, J.S., 1977. Overwash sedimentation associated with a large-scale northeaster. *Marine Geology*, 24(2), 109–121.

Levin, N., 2011. Climate-driven changes in tropical cyclone intensity shape dune activity of the Earth's largest sand island. *Geomorphology*, 125(1), 239–252.

Levin, N.; Neil, D., and Syktus, J., 2014. Spatial variability of dune form on Moreton Island, Australia, and its correspondence with wind regime derived from observing stations and reanalysis. *Aeolian Research*, 15, 289–300.

Luijendijk, A.; Hagenaars, G.; Ranasinghe, R.; Baart, F.; Donchyts, G., and Aarninkhof, S., 2018. The state of the world's beaches. *Scientific Reports*, 8, article 6641, 11p.

Maglione, P.; Parente, C., and Vallario, A., 2014. Coastline extraction using high resolution WorldView-2 satellite imagery. *European Journal of Remote Sensing*, 47(1), 685–699.

Maio, C.V.; Gontz, A.M.; Sullivan, R.M.; Madsen, S.M.; Weidman, C.R., and Donnelly, J.P., 2014. Subsurface evidence of storm-driven breaching along a transgressing barrier system, Cape Cod, USA. *Journal of Coastal Research*, 32(2), 264–279.

Maio, C.V.; Gontz, A.M.; Tenenbaoum, D.E., and Berkland, E.P., 2012. Coastal hazard vulnerability assessment of sensitive histor-

ical sites on Rainsford Island, Boston Harbor, Massachusetts. *Journal of Coastal Research*, 28(1), 20–33.

May, S.M.; Brill, D.; Leopold, M.; Callow, N.; Engel, M.; Scheffers, A.; Opitz, S.; Norpoth, M., and Bruckner, H., 2017. Chronostratigraphy and geomorphology of washover fans in the Exmouth Gulf (NW Australia)—A record of tropical cyclone activity during the late Holocene. *Quaternary Science Reviews*, 169, 65–84.

May, S.M.; Gelhausen, H.; Brill, D.; Callow, J.N.; Engel, M.; Pitz, S.; Scheffers, A.; Joannes-Boyau, R.; Leopold, M., and Brukner, H., 2018. Chenier-type ridges in Giralia Bay (Exmouth Gulf, Western Australia)—Process, chronostratigraphy and significance for recording past tropical cyclones. *Marine Geology*, 396, 186–204.

McSweeney, S. and Shulmeister, J., 2018. Variations in wave climate as a driver of decadal scale shoreline change at the Inskip Peninsula, southeast Queensland, Australia. *Estuarine, Coastal, and Shelf Science*, 209, 56–69.

MHL (Manly Hydraulics Laboratory), 2012. *OEH NSW Tidal Planes Analysis: 1990–2010 Harmonic Analysis*. Sydney, Australia: Manly Hydraulics Laboratory, *Report MHL2053*, 18p.

Miner, M.D.; Kulp, M.A.; FitzGerald, D.M., and Georgiou, I.Y., 2009. Hurricane-associated ebb-tidal delta sediment dynamics. *Geology*, 37(9), 851–854.

Moore, L.J., 2000. Shoreline mapping techniques. *Journal of Coastal Research*, 16(1), 111–124.

Moore, L.J.; Ruggiero, P., and List, J.H., 2006. Comparing mean high water and high water line shorelines: Should proxy-datum offsets be incorporated into shoreline change analysis? *Journal of Coastal Research*, 22(4), 894–905.

Morton, R.A., 1991. Accurate shoreline mapping: Past, present, and future. *In:* Kraus, N.C.; Gingerich, K.J., and Kriebel, D.L. (eds.), *Proceedings of a Specialty Conference on Quantitative Approaches to Coastal Sediment Processes (Coastal Sediments '91)*, vol 1 (Seattle, Washington), pp. 997–1010.

Morton, R.A.; Gibeaut, J.C., and Paine, J.G., 1995. Meso-scale transfer of sand during and after storms: Implications for prediction of shoreline movement. *Marine Geology*, 126(1–4), 161–179.

Overton, M.F. and Fisher, J.S., 1996. Shoreline analysis using digital photogrammetry. *In:* Edge, B.L. (ed.), *Proceedings of the 25th International Conference on Coastal Engineering* (Orlando, Florida), pp. 3750–3761.

Pajak, M.J. and Leatherman, S.P., 2002. The high water line as shoreline indicator. *Journal of Coastal Research*, 18(2), 329–337.

Pardo-Pascual, J.E.; Almonacid-Caballer, J.; Ruiz, L.A.; Palomar-Vazquez, J., and Rodrigo-Alemany, R., 2014. Evaluation of storm impact on sandy beaches of the Gulf of Valencia using Landsat imagery series. *Geomorphology*, 214, 388–401.

Planet, 2017. Planet Imagery Product Specification. San Francisco, CA: Planet Labs, 56p.

Putgatch, T., 2019. Tropical storms and mortality under climate change. *World Development*, 117, 172–182.

Ranasinghe, R.; McLoughlin, R.; Short, A., and Symonds, G., 2004. The Southern Oscillation Index, wave climate, and beach rotation. *Marine Geology*, 204(3–4), 273–287.

Redland City Bulletin, 2019. Beaches left eroded as ex-tropical cyclone Oma impacts on south-east Queensland's coastline. https://www.redlandcitybulletin.com.au/story/5916958/wild-weather-watch-updates/?fbclid=IwAR3uaE-Y4_BbWq8mRGavMhNQeTsqnqe6Z9fY9eInNVcDPTkmKxQLxgCjeiQ

Roy, D.P.; Wulder, M.A.; Loveland, T.R.; Woodcock, C.E.; Allen, R.G.; Anderson, M.C.; Helder, D.; Irons, J.R.; Johnson, D.M.; Kennedy, R.; Scambos, T.A.; Schaaf, C.B.; Schott, J.R.; Sheng, Y.; Vermote, E.F.; Belward, A.S.; Bindschadler, R.; Cohen, W.B.; Gao, F.; Hipple, J.D.; Hostert, P.; Huntington, J.; Justice, C.O.; Kilic, A.; Kovalskyy, V.; Lee, Z.P.; Lymburner, L.; Masek, J.G.; McCorkel, J.; Shuai, Y.; Trezza, R.; Vogelmann, J.; Wynne, R.H., and Zhu, Z., 2014. Landsat-8: Science and product vision for terrestrial global change research. *Remote Sensing of Environment*, 145, 154–172.

Ruggiero, P. and List, J.H., 2009. Improving accuracy and statistical reliability of shoreline position and change rate estimates. *Journal of Coastal Research*, 25(5), 1069–1081.

Sekovski, I.; Stecchi, F.; Mancini, F., and Del Rio, L., 2014. Image classification methods applied to shoreline extraction on very high-resolution multispectral imagery. *International Journal of Remote Sensing*, 35(10), 3556–3578.

Short, A.D.; Trembanis, A.C., and Turner, I.L., 2000. Beach oscillation, rotation and the Southern Oscillation, Narrabeen Beach, Australia. *In:* Edge, B.L. (ed.), *Proceedings of the 27th International Coastal Engineering Conference* (Sydney, Australia), pp. 2439–2452.

Smith, A.W.S. and Jackson, L.A., 1992. The variability in width of the visible beach. *Shore and Beach*, 60(2), 7–14.

Stockdon, H.F.; Holman, R.A.; Howd, P.A., and Sallenger, A.H., Jr., 2006. Empirical parameterization of setup, swash, and runup. *Coastal Engineering*, 53(7), 573–588.

Tejan-Kella, M.S.; Chittleborough, D.J.; Fitzpatrick, R.W.; Thompson, C.H.; Prescott, J.R., and Hutton, J.T., 1990. Thermoluminescence dating of coastal sand dunes at Cooloola and North Stradbroke Island, Australia. *Australian Journal of Soil Research*, 28(4), 465–481.

Thieler, E.R. and Danforth, W.W., 1994. Historical shoreline mapping (I): Improving techniques and reducing positioning errors. *Journal of Coastal Research*, 10(3), 549–563.

Thieler, E.R.; Himmelstoss, E.A.; Zichichi, J.L., and Ergul, A., 2017. *Digital Shoreline Analysis System (DSAS) Version 4.0—An ArcGIS Extension for Calculating Shoreline Change (ver. 4.4, July 2017)*. Reston, Virginia: U.S. Geological Survey, *Open-file Report 2008-1278*.

Thompson, C., 1983. Development and weathering of large parabolic dune systems along the subtropical coast of eastern Australia. *Zeitschrift fur Geomorphologie*, 45, S205–S225.

van der Werff, H.M.A., 2019. Mapping shoreline indicators on a sandy beach with supervised edge detection of soil moisture differences. *International Journal of Applied Earth Observation and Geoinformation*, 74, 231–238.

Vousdoukas, M.I.; Velegrakis, A.F.; Dimou, K.; Zervakis, V., and Conley, D.C., 2009. Wave run-up observations in microtidal, sediment-starved pocket beaches of the Eastern Mediterranean. *Journal of Marine Systems*, 78, S37–S47.

Walker, J.; Lees, B.; Olley, J., and Thompson, C., 2018. Dating the Cooloola coastal dunes of South-Eastern Queensland, Australia. *Marine Geology*, 398, 73–85.

Wasantha, P. and Ranjith, P., 2014. Water-weakening behavior of Hawkesbury sandstone in brittle regime. *Engineering Geology*, 178, 91–101.

Williams, H.F.L., 2015. Contrasting styles of Hurricane Irene washover sedimentation on three east coast barrier islands: Cape Lookout, North Carolina; Assateague Island, Virginia; and Fire Island, New York. *Geomorphology*, 231, 182–192.

Xu, N., 2018. Detecting coastline change with all available Landsat data over 1986–2015: A case study for the state of Texas, USA. *Atmosphere*, 9(3), 107.

Yue, Y.; Yu, K.; Tao, S.; Zhang, H.; Liu, G.; Wang, N.; Jiang, W.; Fan, T.; Lin, W., and Wang, Y., 2019. 3500-year western Pacific storm records warns of additional storm activity in a warm pool. *Palaeogeography, Palaeoclimatology, Palaeoecology*, 521, 57–71.

Zajic, B.N.; Simmon, R.; Mascaro, J.; Kington, J.D., and Jordahl, K.A., 2018. How access to daily medium-resolution satellite imagery can aid the global disaster response community, *Abstract NH23F-3559* presented at 2018 Fall Meeting, AGU (Washington, D.C.), 10–14 December.

Zhang, K.; Douglas, B.C., and Leatherman, S.P., 2004. Global warming and coastal erosion. *Climate Change*, 64, 41–58.

Zhang, K.; Huang, W.; Douglas, B.C., and Leatherman, S.P., 2002. Shoreline position variability and long-term trend analysis. *Shore and Beach*, 70(2), 31–35.

Zhang, K.; Whitman, D.; Leatherman, S., and Robertson, W., 2005. Quantification of beach changes caused by Hurricane Floyd along Florida's Atlantic Coast using airborne laser surveys. *Journal of Coastal Research*, 21(1), 123–134.